

## A theoretical analysis of pitch stability during gliding in flying snakes

This content has been downloaded from IOPscience. Please scroll down to see the full text.

2014 Bioinspir. Biomim. 9 025014

(<http://iopscience.iop.org/1748-3190/9/2/025014>)

View [the table of contents for this issue](#), or go to the [journal homepage](#) for more

Download details:

IP Address: 198.82.18.230

This content was downloaded on 22/05/2014 at 18:04

Please note that [terms and conditions apply](#).

# A theoretical analysis of pitch stability during gliding in flying snakes

Farid Jafari<sup>1</sup>, Shane D Ross<sup>1</sup>, Pavlos P Vlachos<sup>2</sup> and John J Socha<sup>1</sup>

<sup>1</sup>Engineering Science and Mechanics, Virginia Tech, Blacksburg, VA 24061, USA

<sup>2</sup>School of Mechanical Engineering, Purdue University, West Lafayette, IN 47907, USA

E-mail: [jafari@vt.edu](mailto:jafari@vt.edu)


Received 1 November 2013, revised 8 April 2014

Accepted for publication 23 April 2014

Published 22 May 2014

## Abstract

Flying snakes use their entire body as a continuously morphing ‘wing’ to produce lift and shallow their glide trajectory. Their dominant behavior during gliding is aerial undulation, in which lateral waves are sent posteriorly down the body. This highly dynamic behavior, which is unique among animal gliders, should have substantial effects on the flight dynamics and stability of the snakes, resulting from the continuous redistribution of mass and aerodynamic forces. In this study, we develop two-dimensional theoretical models to assess the stability characteristics of snakes in the pitch direction. Previously measured force coefficients are used to simulate aerodynamic forces acting on the models, and undulation is simulated by varying mass. Model 1 is a simple three-airfoil representation of the snake’s body that possesses a passively stable equilibrium solution, whose basin of stability contains initial conditions observed in experimental gliding trajectories. Model 2 is more sophisticated, with more degrees of freedom allowing for postural changes to better represent the snake’s real kinematics; in addition, a restoring moment is added to simulate potential active control. The application of static and dynamic stability criteria show that Model 2 is passively unstable, but can be stabilized with a restoring moment. Overall, these models suggest that undulation does not contribute to stability in pitch, and that flying snakes require a closed-loop control system formed around a passively stable dynamical framework.

 Online supplementary data available from [stacks.iop.org/BB/9/025014/mmedia](http://stacks.iop.org/BB/9/025014/mmedia)

Keywords: flying snakes, gliding, stability, dynamical model

(Some figures may appear in colour only in the online journal)

## List of Symbols

<b>A</b>	Jacobian matrix	$\mathbf{f}_1, \mathbf{f}_2$	forces acting between the airfoils and the middle link in Model 2
$b$	damping coefficient	$f_1, f_2$	the magnitudes of those forces
$B_u$	angular damping coefficient	$\mathbf{f}(\mathbf{x}, \dot{\mathbf{x}})$	forcing term due to undulation
$\mathbf{c}(\mathbf{x}, \dot{\mathbf{x}}, t)$	vector of Coriolis, centripetal and damping terms	$F_l, F_d$	lift and drag forces
$C_l, C_d$	lift and drag coefficients	$\mathbf{F}$	the net external force
$d$	distance between airfoils in Model 1	$\mathbf{F}^*$	the modified force for a variable mass system
$e$	objective function	$g$	acceleration of gravity
		$\mathbf{g}(\mathbf{x}, t)$	vector of elastic and gravitational terms
		$\mathbf{G}$	the linear momentum
		$\mathbf{H}_c$	the angular momentum about CoM

$I_i$	moment of inertia of the middle link	$\mu$	the nondimensional moment of inertia of the middle link in Model 2
$\mathbf{I}$	the identity matrix		
$j$	subscript used for numbering in summations	$\rho_{\text{air}}$	density of air
$k$	elastic coefficient	$\sigma$	the initial phase
$K_u$	angular elastic coefficient	$\tau$	period of $\mathbf{y}_0$
$l$	half of the length of the middle link	$\varphi$	the airfoil angle
$l_{\text{SV}}$	the snake's snout-vent length	$\Phi$	the monodromy matrix
$m_a$	airfoil mass	$\omega$	frequency of undulation
$m_i$	the middle link's mass		
$m_j$	mass of the $j$ th airfoil		
$m_{\text{tot}}$	total mass		
$M_c$	moment about the CoM		
$M_u$	restoring moment		
$\mathbf{M}(\mathbf{x}, t)$	the mass matrix		
$p$	a parameter		
$q_j$	a generalized force		
$\mathbf{q}(\mathbf{x}, \dot{\mathbf{x}}, t)$	vector of the generalized forces		
$r_1, r_2$	distances of the airfoils from the center of the middle link in Model 2		
$r_c, \mathbf{r}_c$	position of the CoM		
$R$	the dissipation energy function		
$S_a$	airfoil area		
$t$	time		
$T$	kinetic energy		
$u, \mathbf{u}$	speed of the mass traveling between the airfoils		
$v$	airfoil speed		
$\mathbf{v}$	airfoil velocity		
$V$	potential energy		
$W$	work of the nonconservative forces		
$x$	position variable		
$x_j$	a generalized coordinate		
$\mathbf{x}$	vector of the generalized coordinates		
$\mathbf{y}$	vector of the state coordinates		
$\mathbf{y}_0$	a periodic solution		
$\tilde{\mathbf{y}}$	a perturbation		
$\tilde{\mathbf{Y}}$	the solution matrix to the perturbed system		
$z$	position variable		
$\alpha_b$	body angle of attack		
$\beta$	summation of the pitch angle and the glide angle		
$\gamma$	the glide angle		
$\delta$	the variational operator		
$\Delta m$	the undulating mass		
$\zeta$	the nondimensional undulating mass		
$\eta_1, \eta_2$	the nondimensional airfoil masses		
$\theta$	the pitch angle		

## 1. Introduction

All flyers require the ability to alter flight speed, trajectory, and body orientation to meet performance objectives such as efficiency and control for straight flight, maneuvering, and landing. Flight control is usually accomplished through asymmetric deployment of aerodynamic surfaces about different body axes (Dudley 2002). From aircraft to animals that have evolved the ability to fly, the use of symmetrically paired wings is an almost universal feature. Elevators, wing flaps, spoilers and a horizontal tail are used in aircraft as control devices, but flying and gliding animals must use their wings, tail and other morphological features both to generate aerodynamic forces and to control the trajectory (Biewener 2003, Alexander 2003).

For most animal gliders, flight control is augmented by the ability to selectively apply forces to counteract rotations, usually by altering wing characteristics (such as camber) or by shifting the position of appendages. However, flying snakes of the genus *Chrysopelea* lack conventional wings and appendages, and possess no specialized anatomy for control. Despite a design that would appear disadvantageous for flight, the glide performance of flying snakes is comparable to that of other gliders (Scholey 1986, McGuire 1998, Socha *et al* 2005), with one species that is even capable of aerial maneuvers (Socha 2002, Socha *et al* 2005, 2010). In contrast, some nonflying snakes are known to tumble when dropped from a height (Heyer 1970), and no other species can glide, demonstrating that the physical or physiological mechanisms of control used by *Chrysopelea* are not present in all snakes. However, the specific mechanisms that enable *Chrysopelea* snakes to remain stable while gliding, or to turn on command, are unknown.

Recent studies have helped to elucidate the basic kinematic features of glide trajectories of flying snakes (Socha 2002, 2011, Socha *et al* 2005, 2010, Socha and LaBarbera 2005). After a jumping take-off, the snake passes through a ballistic dive phase, in which the glide angle (the angle of the glide path relative to horizontal) is steep (~50–70°, depending on species) and on the order of 2 m of height is lost. This is followed by a shallowing glide phase in which the glide angle decreases due to lift generation and the glide behavior of the snake develops fully. By the start of this phase, the snake has dorsoventrally flattened its whole body and undulates laterally in an S-like shape, sending traveling

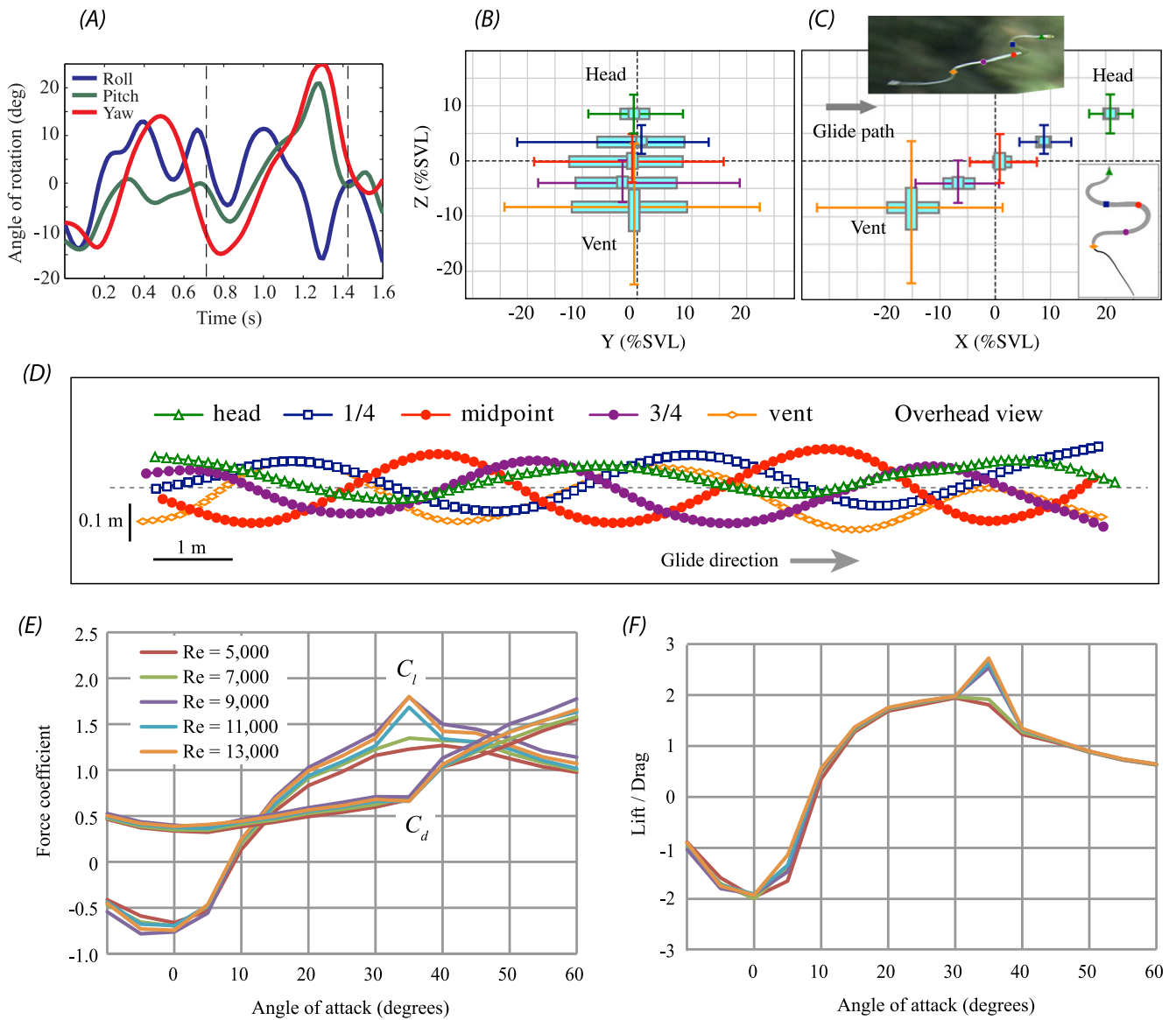


**Figure 1.** Kinematic (A)–(D) and aerodynamic (E), (F) data that were used in this study. (A) Observed rotation angles between an inertial frame and the principal axes of inertia of the snake show that the snake undergoes relatively small roll and pitch angles during gliding. (B) Summary of body posture of *C. paradisi*, in the trajectory reference frame and normalized by SVL from the front view, indicate that the snakes undergo small roll displacement. (C) The side view shows the staggered configuration of flying snakes during glide. These data are composed of the 3D position of five landmarks relative to the CoM of the snake body. (D) The sinusoidal movement of all five landmarks is shown in the overhead view of a trajectory, where the  $y$ -axis is expanded relative to the  $x$ -axis to better reveal side-to-side movements. The kinematic data in (B)–(D) are from late-phase gliding trajectories of eight glide trials performed by two *C. paradisi* snakes (Socha et al 2010). The box plots indicate the mean, and first and third quartiles, with whiskers representing 10% and 90% percentiles. (E) Steady-state lift and drag coefficients measured for a straight airfoil having the same cross-sectional shape as the flattened snake; and (F) lift-to-drag ratio for the same configuration. The aerodynamic data (E), (F) are adapted from (Holden et al 2014).

waves posteriorly down the body (figure 1(D)). During the shallowing phase, the snake maintains a staggered configuration, with the anterior body oriented roughly level to the ground and the overall body angled upward in the range of  $25^\circ$  from the glide path (figure 1(C)). Recent experimental and computational modeling studies show that the snake's body cross-sectional shape can maintain high lift at angles of attack as large as  $35^\circ$ , with lift coefficients reaching as high as 1.9 (figure 1(E)) (Miklasz et al 2010, Holden et al 2014, Krishnan et al 2014). Moreover, high lift and lift-to-drag ratios can be maintained over a large range of angles of attack

(figure 1(F)), helping to explain how the snake begins to generate significant aerodynamic forces even during the steep ballistic dive portion of the trajectory.

Despite our growing understanding of the kinematics and aerodynamics of flying snakes, their ability to maintain flight control remains a mystery. How does an undulating glider produce stable gliding in the absence of obvious control surfaces? An important step toward solving this problem is to understand the snake's stability characteristics in the pitch, roll and yaw directions. The simplest hypothesis is that a flying snake is passively stable in all directions; at the other

extreme, the snake requires active control to counteract rotations about all axes.

Here, we develop new theoretical models as tools to address the stability characteristics of flying snakes for the first time. As a first-order study of a highly complex system, we chose to simplify the problem by considering the snake as a series of 2D airfoils, and focus only on stability in the pitch direction. We conducted simulations of glide trajectories using the aerodynamic characteristics of the snake's cross-sectional shape, with undulation simulated by periodically varying the mass and area of the airfoils. The models were examined for pitch stability by obtaining the eigenvalues of the linearized system about the steady-state solutions.

Overall, we aim to understand the fundamental control mechanisms that snakes employ during a glide, contributing to our broader goal of discovering the minimum set of parameters necessary to reproduce the glide performance of flying snakes. Such work will lend insight to the morphological and behavioral requirements to evolve gliding in snakes, and can also contribute to design principles for future flying snake-inspired air or water vehicles. For example, this work could serve as the basis for a staggered-wing micro-air vehicle that operates in the same Reynolds number regime as the real snake. This vehicle would draw inspiration from the undulating movement of the snake's body, allowing the staggered foils to change their relative spacing in order to achieve a desired aerodynamic performance.

## 2. Methods

Several approaches have been used to assess flight stability of animal flyers. One of the most common methods is to examine the static stability criterion (Etkin 1972, McCormick 1976). When a system experiences a small perturbation from equilibrium, this criterion determines if the acting forces would restore the system back to the equilibrium state. In recent years, the static stability criterion has been used to analyze animal flyers, including the testing of physical models in wind tunnels to understand flying frogs (McCay 2001) and theoretical analyses of how the pitching moment about the center of mass (CoM) changes with angle of attack in birds (Thomas and Taylor 2001). Other studies have examined dynamic stability using kinematics of the moving animal, as has been used to assess insects (Taylor and Thomas 2003) and flying squirrels (Bishop 2006). Computational or robotic models have been used to analyze the passive dynamic stability of hovering fruit flies (Gao *et al* 2011) and hawkmoths (Cheng *et al* 2011).

Most such studies involve the simplifying assumption of bilateral symmetry (but see Gao *et al* 2011), which allows the motions in the longitudinal direction to be decoupled from those in the lateral direction. This enables pitch stability to be considered as a simple one-dimensional problem. McCay (2001) and Thomas and Taylor (2001) additionally considered equilibrium gliding and determined whether disturbances from equilibrium would be passively counteracted.

However, neither of these assumptions can be employed to simplify the problem of gliding in snakes. First, the S-like posture of the snake endows it with a complete lack of bilateral symmetry, which means that the longitudinal and lateral dynamics cannot be decoupled. Second, due to the snake's dynamic undulating motion, whose effect acts like a periodic inertial force, it is unlikely that flying snakes glide in equilibrium. In fact, most recorded glide trajectories consist of transient motion, and equilibrium gliding has rarely been observed (Socha 2002, Socha *et al* 2005, 2010, Socha and LaBarbera 2005). The undulatory motion must periodically change the locations of the center of pressure (CoP) and CoM via redistribution of area and mass, which leads to the hypothesis that the stability characteristics of the snakes are influenced by undulation. Overall, these characteristics suggest that understanding how flying snakes glide requires analyses of both static and dynamic stability.

In this study, we examined the dynamics and stability of gliding flight in snakes by developing two theoretical models, beginning with a simple model and progressing to a more complex and realistic model. As a first-order modeling approach, we ignored the effects of coupling between the longitudinal and lateral dynamics. This can also be viewed as a specific case of a straight glide with negligible roll, for which the longitudinal dynamics are independent from lateral motions.

How justifiable is this approach given real snake glide dynamics? The existing kinematic data are insufficient to appraise the decoupling of longitudinal and laterally dynamics, but lateral motions are indeed negligible under certain conditions. For a straight glide, sideslip and yaw are negligible, and if we also assume that roll is not pronounced, the coupling effects are further diminished. According to figure 1(A), which shows the rotation angles of the body relative to an inertial frame estimated from experimental data (Socha *et al* 2010) for approximately two undulation periods, the assumption of small roll motion is reasonable, at least during late-phase gliding in *Chrysopelea paradisi*. The angles in figure 1(A) are defined as the consecutive rotation angles that transform the inertial frame into the principal axes of inertia of the snake body as a whole; these were calculated from the moments of inertia in the  $x$ - $y$ - $z$  coordinates, which were estimated by assuming that the snake consisted of four line segments of equal masses determined by the 3D coordinates of five landmarks (figure 1(C)). Figure 1(A) shows that for the majority of the time, deviations in roll are less than  $10^\circ$ . Small roll angle could also be inferred from figure 1(B), where the relative displacements of different landmarks on the body are shown in the vertical and lateral directions.

### 2.1. Modeling of forces

We considered gravity and the aerodynamic forces of lift and drag in our two models. To calculate aerodynamic forces, we used lift and drag coefficients ( $C_l$  and  $C_d$ , respectively) from an experimental study of the 2D cross-sectional shape of *C. paradisi*, which assumed steady-state lift and drag (Holden

et al 2014). These coefficients (figures 1(E), (F)) represent values over a range of Reynolds numbers that have been reported for *C. paradisi* (Socha et al 2005). Based on an average glide speed of  $8.9 \pm 1.4 \text{ m s}^{-1}$  (Socha et al 2005) and a characteristic length of 2.2 cm (chord length, Miklasz et al 2010), we chose  $C_l$  and  $C_d$  values corresponding to  $\text{Re} = 11\,000$ .

The use of steady-state aerodynamic force coefficients to model undulating snakes is not ideal, but these coefficients are a reasonable approximation to use in our first-order modeling. As explained in detail by Holden et al (2014), the speed of the snake's forward motion in gliding is much greater than the motions of undulation, which suggests that the freestream velocity should dominate the local airflow patterns over the body. This suggests that it is reasonable to use these force coefficients in a first study. Future modeling should incorporate unsteady and tandem aerodynamic effects on the snake, when such results become available.

## 2.2. Model 1

In the first model, we considered the snake as three evenly spaced airfoils (figure 2). These airfoils represent sections of the snake's body whose long axis (span) is roughly perpendicular to the direction of motion. The distance  $d$  between the airfoils (figure 2(A)) can be characterized as half of the undulation wavelength (figure 2(B)). We restrict the airfoils to remain coplanar. The previously measured kinematics of body movements (Socha et al 2010) justifies this restriction, showing that total displacements of several landmarks on the snake's body, perpendicular to the 'mean' body orientation, are about 10% of the snout-vent length (figure 1(C)). Because no data are available about the local angles of attack along the snake body, as a reasonable first approximation we assumed that the airfoil orientation could be differentiated from the pitch angle  $\theta$  by the same constant angle  $\varphi$  for all of the airfoils (figure 2(A)). The angle  $\varphi$  represents the angle between the chord line of each airfoil and the line that defines the whole-body orientation (i.e., the three-foil system). Further, we assumed that mass and pressure are uniformly distributed along the 'wings'. The basic assumption for the aerodynamics of this model is that the main contribution to producing force comes from those parts of the body that are perpendicular to the air flow, and that the curved portions contribute negligible force.

To simulate undulation, we allowed the masses and, proportionally, areas of the segments to vary as the following functions of time:

$$\begin{cases} m_1(t) = m_a + \Delta m \cos \omega t \\ m_2(t) = m_{\text{tot}} - 2m_a \\ m_3(t) = m_a - \Delta m \cos \omega t \end{cases} \quad (1)$$

where  $\omega$  is the frequency of undulation and  $m_{\text{tot}}$  is the total mass of the snake, with  $m_1(t) + m_2(t) + m_3(t) = m_{\text{tot}}$ . The constraint  $\Delta m < m_a$  applies to equation (1).

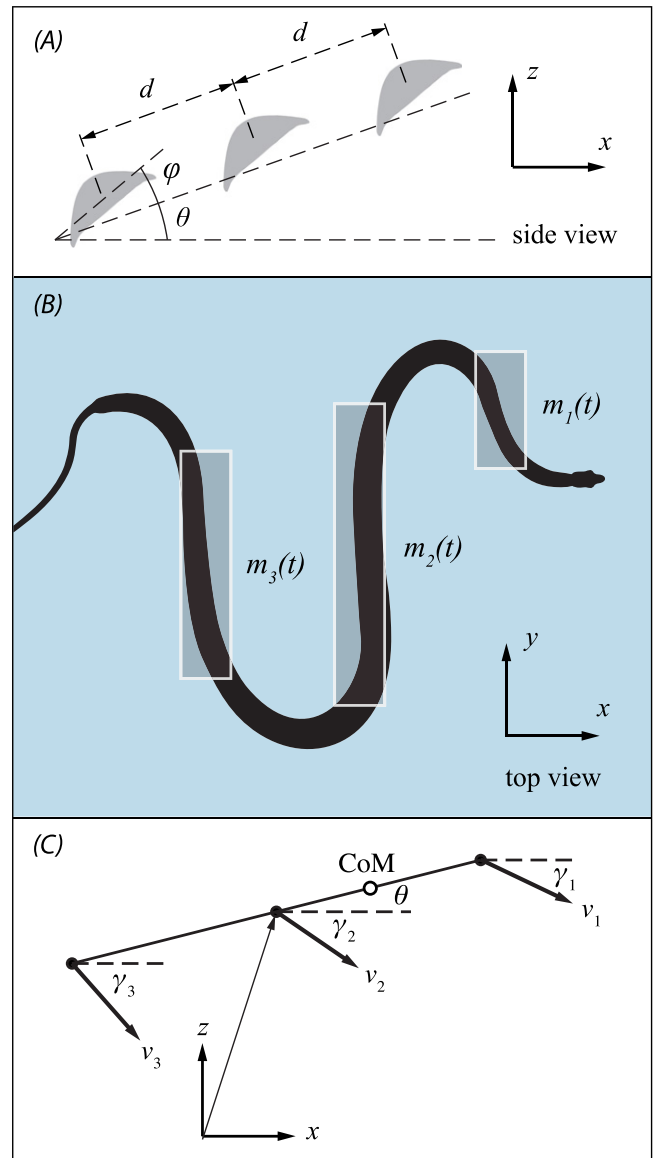


**Figure 2.** (A) 2D structure of Model 1, which is composed of three coplanar airfoils; the distance between the airfoils is constant. (B) Correspondence between the airfoils and parts of the undulating snake body that are perpendicular to the airflow. (C) Kinematics of the model showing the asymmetric effect of pitch velocity on the velocity of airfoils. Resulting from this asymmetry, each airfoil experiences a different glide angle  $\gamma_j$ . The middle airfoil is used as the positional reference point.

The equations of motion of Model 1, whose kinematics are shown in figure 2(C), are written as:

$$\begin{aligned} & m_{\text{tot}} (\ddot{x}\mathbf{i} + \ddot{z}\mathbf{j}) - 2\Delta m d \cos \omega t \\ & \times \left[ \left( \ddot{\theta} \sin \theta + \dot{\theta}^2 \cos \theta \right) \mathbf{i} + \left( -\ddot{\theta} \cos \theta + \dot{\theta}^2 \sin \theta \right) \mathbf{j} \right] \\ & = \sum \left( F_{ij} \sin \gamma_j - F_{dj} \cos \gamma_j \right) \mathbf{i} \\ & \quad + \left( F_{ij} \cos \gamma_j + F_{dj} \sin \gamma_j - m_j g \right) \mathbf{j} \end{aligned} \quad (2)$$

**Table 1.** Initial conditions used for simulations resulting in figures 4–6.

Variable	Figure 4	Figure 5	Figure 6(A)
$x$ (m)	0	0	0
$z$ (m)	10	0	10
$\theta$ (deg)	-30, -10, 0	-8.85	-30–60
$r_1$ (m)	$l$	$l$	
$r_2$ (m)	$l$	$l$	
$\dot{x}$ (m s <sup>-1</sup> )	1.7	6.91	1.7
$\dot{z}$ (m s <sup>-1</sup> )	0	-5.06	0
$\dot{\theta}$ (deg s <sup>-1</sup> )	0	-25.6	-120–120
$\dot{r}_1$ (m s <sup>-1</sup> )	0	0	
$\dot{r}_2$ (m s <sup>-1</sup> )	0	0	

$$2 \left[ \frac{m_a}{m_{\text{tot}}} - \left( \frac{\Delta m}{m_{\text{tot}}} \right)^2 \cos 2\omega t \right] m_{\text{tot}} d^2 \ddot{\theta} = \sum d_j \left( F_{ij} \cos(\theta + \gamma_j) + F_{dj} \sin(\theta + \gamma_j) \right) \quad (3)$$

where  $g$  is the gravitational acceleration,  $d_j$  is the position of airfoils relative to CoM along the longitudinal axis of the body, and  $\gamma_j$  is the glide angle of each airfoil. See the supplementary materials (available at [stacks.iop.org/BB/9/025014/mmedia](http://stacks.iop.org/BB/9/025014/mmedia)) for the detailed derivation of these equations. The lift and drag forces were calculated as:

$$\begin{cases} F_{ij} = \rho_{\text{air}} C_{ij} v_j^2 S_{aj} / 2 \\ F_{dj} = \rho_{\text{air}} C_{dj} v_j^2 S_{aj} / 2 \end{cases} \quad (4)$$

where  $C_{ij}$  and  $C_{dj}$  are the force coefficients, and  $S_{aj}$  is the area of each airfoil.

Equations (2) and (3), together, determine the trajectory of the model when released from any initial position. In the simulations, we set  $\varphi$  equal to the value given in table 2 (see section 2.6 for details).

To study the steady-state behavior of Model 1, we first observe that the equations of motion are nonautonomous, i.e. they explicitly depend on time. Although nonautonomous systems are not usually expected to have equilibrium solutions, we note that with  $\dot{\theta} = 0$ , the airfoils have the same velocity and experience the same angle of attack (see supplementary materials, available at [stacks.iop.org/BB/9/025014/mmedia](http://stacks.iop.org/BB/9/025014/mmedia)). By substituting equation (4) into the right-hand side of equation (3), it can be readily shown that, in this case, CoP coincides with CoM; therefore, the net moment about CoM vanishes and equation (3) is identically satisfied. Also, equation (2) reduces to:

$$m_{\text{tot}} (\ddot{x} \mathbf{i} + \ddot{z} \mathbf{j}) = (F_l \sin \gamma - F_d \cos \gamma) \mathbf{i} + (F_l \cos \gamma + F_d \sin \gamma - m_{\text{tot}} g) \mathbf{j} \quad (5)$$

where  $F_l$  and  $F_d$  are the net lift and drag forces acting on the model and are not explicitly time-dependent.

Equation (5) is equivalent to the equations of motion for a fixed-shape glider, resulting in definite values for equilibrium speed and glide angle. The stability of the equilibrium solution depends on the initial conditions from which the trajectory starts; therefore, the equilibrium is locally stable. Additionally, it is passively stable because stability is inherent in the model's behavior without using closed-loop feedback control.

### 2.3. Model 2

Model 2 was developed based on the idea that the snake maintains a staggered configuration in mid-air, but different parts of the body move relative to one another. In this 2D model, illustrated in figure 3, two airfoils are connected through a rigid link by means of multiple springs and dampers. The airfoils and the long axis of the middle link are restricted to remain collinear, but they are free to move with respect to each other under the action of gravity, aerodynamic forces, and the springs and dampers. The effect of the springs and dampers is shown in figure 3(A) by the forces  $\mathbf{f}_1$  and  $\mathbf{f}_2$ , which have magnitudes:

$$\begin{cases} f_1 = k(r_1 - l) + b\dot{r}_1 \\ f_2 = k(r_2 - l) + b\dot{r}_2 \end{cases} \quad (6)$$

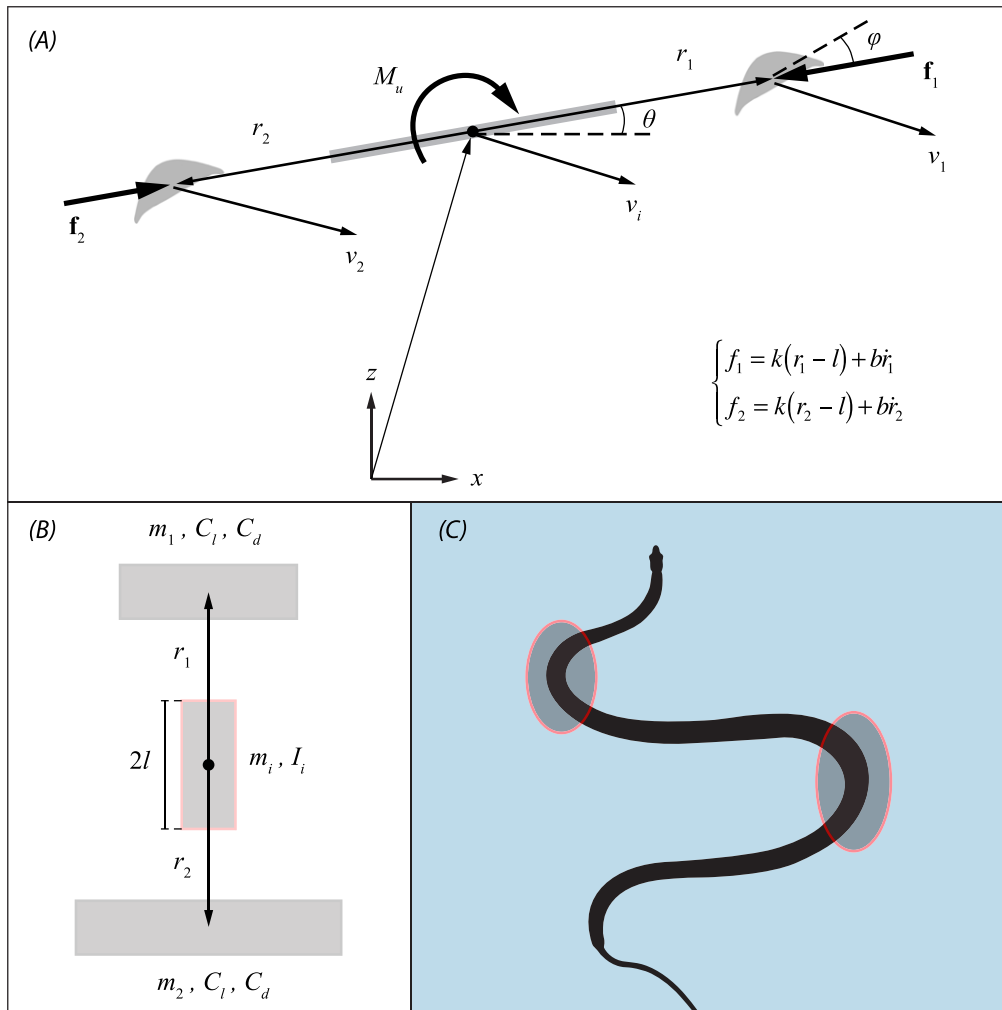
where  $l$  is half of the length of the middle link and the free length of the connecting springs.

Figure 3(B) depicts a top view of Model 2. Compared to Model 1, the middle link is added in this model to represent the role of the parts of the body of the snake that are almost parallel to the direction of motion (figure 3(C)), which provides rotational inertia. Based on the assumption that aerodynamic forces are mainly produced by segments that are perpendicular to the flow, we ignored the aerodynamic contribution from this streamwise middle link. Another modification in Model 2 is that only two airfoils are used, in contrast to three airfoils in Model 1. Because the middle airfoil in Model 1 had no role in the equations of motion, it was removed in Model 2 for the sake of abstraction. The two remaining airfoils were sufficient to produce external forces and moments; therefore, the dynamics of the snake could be adequately approximated by Model 2.

Two more assumptions are present in the construction of Model 2, which are also used in Model 1: (i) the airfoils are constrained to move only along the orientation of the middle link, and (ii) the airfoils have the same angle of attack. Similar to Model 1, the effects of undulation were modeled by allowing the mass of the airfoils to change sinusoidally, such that the total mass of the system remains constant:

$$\begin{cases} m_1(t) = m_{a1} + \Delta m \cos(\omega t + \sigma) \\ m_2(t) = m_{a2} - \Delta m \cos(\omega t + \sigma) \end{cases} \quad (7)$$

where  $\sigma$  is some phase angle and is considered to account for the phase within the undulation cycle at the starting point. Application of equation (7) is subject to the restriction that  $\Delta m < m_{a1}$ ,  $m_{a1}$ . The mass of the middle link  $m_i$  is held fixed.



**Figure 3.** (A) Model 2 from side view, showing that it is composed of two airfoils connected through a middle link by means of springs and dampers. A restoring moment  $M_u$  is used to control the orientation angle  $\theta$  about zero. The center of the middle link is used as the positional reference point. (B) Overhead view of Model 2. (C) The middle link is included in the model to represent the encircled parts of the snake body. These parts are assumed to not contribute to aerodynamic forces, but do provide rotational inertia.

We further assume that the areas of the airfoils are proportional to their masses.

In the previous section, Model 1 was shown to possess locally stable equilibrium solutions, because its structure allowed a uniform distribution of aerodynamic forces. However, in Model 2, presence of the middle link, which does not produce any aerodynamic forces, makes it impossible that such a solution be obtained. Therefore, active control is required in Model 2 to stabilize the trajectories. We used a restoring moment in Model 2 to represent the overall effect of control movements. Based on kinematic observations showing that the snake's body remains roughly level with the ground in mid-glide (Socha *et al* 2010), a linearized form was considered for the restoring moment, which would maintain the pitch angle  $\theta$  close to zero. Similar to expressions that have been commonly used to stabilize models of flying animals (see e.g. Cheng *et al* 2011), we let:

$$M_u = K_u \theta + B_u \dot{\theta} \quad (8)$$

It is important to note that the proportionality term  $K_u \theta$  might not be sufficient for control, because it could over-compensate to disturbances and lead to divergent oscillations. Therefore, a damping term  $B_u \dot{\theta}$  was also included to dissipate the unwanted pitching motion.

#### 2.4. Equations of motion for Model 2

Before deriving the equations of motion, a few definitions are presented for convenience of notation. We select  $\mathbf{x} = [x \ z \ \theta \ r_1 \ r_2]^T$  (see figure 3(A)) as the vector of generalized coordinates of the system. Among these variables,  $x$  and  $z$  define the position of the model as a whole in the plane of motion and are called the position variables, while  $r_1$ ,  $r_2$  and  $\theta$  determine the relative position of model segments and are called the configuration



variables. Additionally, we define the state vector as:

$$\mathbf{y} = [\theta \ r_1 \ r_2 \ \dot{x} \ \dot{z} \ \dot{\theta} \ \dot{r}_1 \ \dot{r}_2]^T \quad (9)$$

The reason for excluding the position variables from the state vector is that, unlike state variables, they will not settle to periodic motions, and prevent obtaining a periodic steady-state solutions (see section 2.6 for more details).

The equations of motion are derived using a Lagrangian formulation, and are written in the following matrix form:

$$\begin{aligned} \mathbf{M}(\mathbf{x}, t) \ddot{\mathbf{x}} + \mathbf{c}(\mathbf{x}, \dot{\mathbf{x}}, t) + \mathbf{g}(\mathbf{x}, t) \\ = \mathbf{q}(\mathbf{x}, \dot{\mathbf{x}}, t) + \mathbf{f}(\mathbf{x}, \dot{\mathbf{x}}) \sin(\omega t + \sigma) \end{aligned} \quad (10)$$

where  $\mathbf{M}(\mathbf{x}, t)$  is the mass matrix,  $\mathbf{c}(\mathbf{x}, \dot{\mathbf{x}}, t)$  is a vector containing the centrifugal, Coriolis and damping terms,  $\mathbf{g}(\mathbf{x}, t)$  contains the gravitational and elastic terms, and  $\mathbf{q}(\mathbf{x}, \dot{\mathbf{x}}, t)$  is the vector of generalized force. Also,  $\mathbf{f}(\mathbf{x}, \dot{\mathbf{x}})$  is a forcing term produced by the transport of mass between the airfoils, whose harmonic behavior is shown in equation (10).

Upon integration of equation (10) from any initial condition, the glide trajectory of the model can be determined. A detailed derivation of equation (10) including explicit formulae for the terms is provided in the supplementary materials (available at [stacks.iop.org/BB/9/025014/mmedia](http://stacks.iop.org/BB/9/025014/mmedia)).

### 2.5. Determination of parameters for Model 2

It can be seen from figure 3 and equations (6)–(8) that Model 2 involves multiple parameters, including the inertial parameters  $m_{a1}$ ,  $m_{a2}$ ,  $\Delta m$ ,  $m_i$  and  $I_i$ ; biomechanical parameters  $k$  and  $b$ ; geometric parameters  $l$ ,  $\sigma$  and  $\varphi$ ; and control parameters  $K_u$  and  $B_u$ . Among these, determining  $K_u$  and  $B_u$  required fitting the model to observed glide trajectories of snakes, by formulating it as an optimization problem (see below). This approach has been commonly used when control system parameters are dealt with; for example, Cheng *et al* (2011) determined the characteristic coefficients of the feedback control system of a hawkmoth model using a similar approach. Because direct measurement of other parameters from live specimens of flying snakes was not possible for this study, we chose to use a data fitting procedure to find model parameters by requiring that the resulting model would reproduce the observed glide trajectories as close as possible.

We chose to use glide trajectory data from a previous study (Socha *et al* 2010), using a representative snake 42.0 g in mass and 74.0 cm in snout-vent length (SVL). Based on another study (Socha *et al* 2005) and following Miklasz *et al* (2010), we estimated that this snake created an airfoil with a chord of 2.2 cm by flattening its body.

To simplify the formulation, the following non-dimensionalized inertial parameters were used in the process:

$$\begin{cases} \eta_1 = m_{a1}/m_{tot} \\ \eta_2 = m_{a2}/m_{tot}, \quad \mu = \frac{I_i}{m_i l^2/3} \\ \zeta = \Delta m/m_{tot} \end{cases} \quad (11)$$

Equation (7) could then be rewritten as:

$$\begin{cases} m_1 = [\eta_1 + \zeta \cos(\omega t + \sigma)] m_{tot} \\ m_2 = [\eta_2 - \zeta \cos(\omega t + \sigma)] m_{tot} \end{cases} \quad (12)$$

We thus obtain the mass and moment of inertia of the middle link as:

$$m_i = (1 - \eta_1 - \eta_2) m_{tot} \quad (13a)$$

$$I_i = \mu (1 - \eta_1 - \eta_2) \frac{1}{3} m_{tot} l^2 \quad (13b)$$

Using the assumption that the projected areas of the airfoils are proportional to their masses, we could also find the airfoil area  $S_a$  from equation (12):

$$S_{aj} = \frac{m_j}{m_{tot}} l_{SV} c, \quad j = 1, 2 \quad (14)$$

where  $l_{SV}$  and  $c$  are SVL and airfoil chord, respectively.  $S_a$  is used along with the aerodynamic coefficients to calculate the lift and drag forces.

Finally, the error between the recorded trajectory and the theoretical trajectory obtained by integration of equation (10) is defined in the least squares sense as:

$$e = \int_{t_1}^{t_2} [(x_r(t) - x_m(t))^2 + (z_r(t) - z_m(t))^2] dt \quad (15)$$

where the subscripts  $r$  and  $m$  denote the recorded and model trajectories, respectively. The model parameters are the solution to an optimization problem in which the error in equation (15) is considered as the objective function to be minimized.

It is important to note that the discretized form of equation (15) was used here, because the measured data existed at a series of discrete time steps. We used the initial conditions based on the previous trajectory data (table 1). We chose initial values of  $x$ ,  $z$  and  $\theta$  from the measured data, whereas the initial values of  $\dot{x}$ ,  $\dot{z}$  and  $\dot{\theta}$  were calculated using a finite difference formula. Because no measured data existed for  $r_1$  and  $r_2$ , we simply integrated these variables from rest ( $r_1 = r_2 = l$  and  $\dot{r}_1 = \dot{r}_2 = 0$ ).

### 2.6. Stability analysis

To analyze the stability characteristics of a system in the sense of dynamic stability, we first need to determine its steady-state response. Model 2, as described by equation (10), is nonautonomous and periodically forced with the frequency of undulation. Hence, the steady-state response of Model 2 is periodic in state space and has the same frequency. As a side note, it should now be clear that in order to be able to obtain periodic solutions, we had to define the state vector as in equation (9), because the trajectory in the  $x$ - $z$  plane is not periodic. We can assess the stability of the periodic solution by applying the Floquet theory (Nayfeh and Balachandran 2004), which is described below.

Due to the complexity of the equations of motion of Model 2, analytical solutions were not attempted; instead, we

employed a finite difference method to determine the solution to equation (10). First, a sufficiently small step size was selected to construct a dense set of time steps spanning one period of undulation. Then, a central difference formula was used to approximate the time derivative of the state vector at the midpoint of each interval. By imposing the periodicity condition, a set of algebraic equations was obtained in terms of discrete states at the steps, sufficient to solve for discrete states, determining the periodic solution (Nayfeh and Balachandran 2004). This periodic solution is called  $\mathbf{y}_0(t)$ , and we denote its period by  $\tau$ .

To examine the dynamic stability of  $\mathbf{y}_0(t)$ , equation (10) is first rewritten in the following state space form:

$$\dot{\mathbf{y}} = \hat{\mathbf{y}}(\mathbf{y}, t; p) \quad (16)$$

where  $p$  could be any parameter. A disturbance  $\tilde{\mathbf{y}}(t)$  is superimposed on  $\mathbf{y}_0(t)$ , so that:

$$\mathbf{y}(t) = \mathbf{y}_0(t) + \tilde{\mathbf{y}}(t) \quad (17)$$

Next, equation (17) is substituted into equation (16), a Taylor series expansion is used about  $\mathbf{y}_0(t)$ , and linear terms in the disturbance are retained. It follows that:

$$\dot{\tilde{\mathbf{y}}} = \left. \frac{\partial \hat{\mathbf{y}}}{\partial \mathbf{y}} \right|_{\mathbf{y}_0} \tilde{\mathbf{y}} = \mathbf{A}(t; p) \tilde{\mathbf{y}} \quad (18)$$

where  $\mathbf{A}(t; p)$  is the Jacobian matrix. The linearly independent solutions of equation (18) are collected in a matrix form as below:

$$\tilde{\mathbf{Y}}(t) = [\tilde{\mathbf{y}}_1(t) \ \tilde{\mathbf{y}}_2(t) \ \dots \ \tilde{\mathbf{y}}_8(t)] \quad (19)$$

$\tilde{\mathbf{Y}}(t)$  is the fundamental matrix solution and satisfies the differential equation:

$$\dot{\tilde{\mathbf{Y}}}(t) = \mathbf{A}(t; p) \tilde{\mathbf{Y}}(t) \quad (20)$$

When integrated from the initial condition  $\tilde{\mathbf{Y}}(0) = \mathbf{I}$ , the fundamental matrix solution evaluated at the period  $\tau$  is called the monodromy matrix; i.e.

$$\Phi = \tilde{\mathbf{Y}}(\tau), \quad (21)$$

The eigenvalues of the monodromy matrix,  $\Phi$ , are called Floquet multipliers. The Floquet theory states that stability of  $\mathbf{y}_0(t)$  is determined by the following condition: if all of the Floquet multipliers are within the unit circle in the complex plane, the periodic solution is stable (Nayfeh and Balachandran 2004).

The effect of parameter  $p$  on the stability of  $\mathbf{y}_0(t)$  can be determined by examining whether changes in the value of  $p$  cause a Floquet multiplier to enter or exit the unit circle. For the case of Model 2, parameters of interest are  $K_u$  and  $B_u$ , and  $\Delta m$  (or equivalently  $\zeta$ , which is a measure of undulating amplitude and could be used to determine the effect of undulation on the pitch stability of the model). A previous study of flying snake kinematics (Socha and LaBarbera 2005) found no correlation between undulation frequency and any glide performance variable. Therefore, we do not consider

this parameter here. Among the parameters of interest, the amplitude of undulation,  $\zeta$ , requires further elaboration, because the forcing term  $\mathbf{f}(\mathbf{x}, \dot{\mathbf{x}})$  is proportional to it; see equation (S21). As this parameter goes to zero, the steady-state response continuously transforms from a periodic to an equilibrium solution, for which the Floquet theory can no longer be applied. In this case, the eigenvalues associated with the linearized equations of motion have to be obtained; for an equilibrium solution to be dynamically stable, all of these eigenvalues must have negative real parts (Nayfeh and Balachandran 2004).

Here, for an equilibrium solution of Model 2 with  $\zeta = 0$  (i.e., without undulation), we instead applied the static stability criterion, which determines the ability of a system to produce a restoring effect after receiving a disturbance, and is a necessary condition for dynamic stability. In planar motion, the analysis of static stability in the pitch direction reduces to determining the slope with which pitching moment,  $M_c$ , varies with angle of attack,  $\alpha_b$ . If the slope is negative, i.e.

$$\frac{\partial M_c}{\partial \alpha_b} < 0, \quad (22)$$

this means that a disturbance from equilibrium passively induces an opposing pitching moment, and the system is statically stable (Taylor and Thomas 2002). This criterion was applied to Model 2 without undulation as follows:

We kept the pitch angle  $\theta$  constant, integrated equation (10) with respect to other generalized coordinates, giving sufficient time to let them reach steady-state. Then, the reference angle of attack was found as:

$$\alpha_b = \theta - \tan^{-1}(\dot{z}/\dot{x}) \quad (23)$$

Also, the pitching moment was obtained as:

$$M_c = (r_1 - r_c)(F_{l1} \cos \beta_1 + F_{d1} \sin \beta_1) - (r_2 + r_c)(F_{l2} \cos \beta_2 + F_{d2} \sin \beta_2) - K_u \theta \quad (24)$$

with  $\beta_j$ ,  $j = 1, 2$  defined in equation (S15), and  $r_c$  being the position of CoM with respect to the center of the middle link, calculated as:

$$r_c = (m_1 r_1 - m_2 r_2) / m_{tot} \quad (25)$$

By repeating the above procedure while changing the pitch angle, a curve is constructed displaying the relation between the pitching moment and angle of attack. The stability criterion of equation (22) was applied to this curve. For comparison, this criterion was also applied to the model with undulation. For this case, the reference angle of attack and the pitching moment had to be averaged over one period of undulation. Finally, we varied  $K_u$  to examine the effect of the control term on the static stability properties of the system.

### 2.7. Simulations

We used custom-written programs in MATLAB (version 2010a) to integrate the equations of motion (using ode functions), to solve the parameter-fitting problem (formulated

**Table 2.** The model parameters fitted to experimental data along with the lower and upper bounds used in the optimization process.

Parameter	Fitted value	Lower bound	Upper bound
$\eta_1$	0.379	0.2	0.4
$\eta_2$	0.380	0.2	0.4
$\zeta$	0.319	0.25	0.35
$l/c$	2.981	1	4
$\mu$	0.495	0	2
$k$ (N m <sup>-1</sup> )	0.198	0	2
$b$ (Ns m <sup>-1</sup> )	0.199	0	2
$K_u$ (Nm rad <sup>-1</sup> )	0.119	0	2
$B_u$ (Nms rad <sup>-1</sup> )	0.099	0	2
$\varphi$ (deg)	-5.39	-30	30
$\sigma$ (deg)	3.92	-180	180

as an optimization problem and solved using the `fmincon` function) and to perform the subsequent simulations. The sequential quadratic programming algorithm was employed to solve the optimization problem and to find the unknown model parameters within a definite range determined by lower and upper bounds. These bounds were imposed on the solution to ensure a biomechanically realistic solution. The optimization process resulted in several local minima of the error function, among which we selected the solution associated with the least error value.

We carried out several simulations with the developed models, using initial conditions that are summarized in table 1. In addition, we used  $m_a = m_{tot}/4$  and  $\Delta m = m_{tot}/4$  for Model 1. The fitted parameters for Model 2 are given in table 2 along with the lower and upper bounds against which they were obtained. For consistency, the value of  $\varphi$  obtained for Model 2 was used for both models in all simulations.

### 3. Results

#### 3.1. Trajectory simulations

To investigate how the developed theoretical models predict the transition from the ballistic phase to the shallowing phase, the trajectories and corresponding glide angles starting from  $(\dot{x}_0, \dot{z}_0) = (1.7, 0) \text{ m s}^{-1}$  were compared to the experimental trajectories in Socha *et al* (2005) (figures 4(A) and (B)). Because no data exist on the initial pitch angle of the snake, we assumed reasonable values for the simulations. Figure 4(A) shows that Model 1 with  $\theta_0 = -10^\circ$  produced a trajectory that followed the experimental data; it also shows that the trajectories predicted by Model 1 do not change monotonically with  $\theta_0$ . When the initial pitch angle is decreased from zero to  $\theta_0 = -10^\circ$ , the distance traveled increased by about 20%; but if  $\theta_0$  is further decreased to  $\theta_0 = -30^\circ$ , the traveled distance is less than halved. Figure 4(B) shows that no shallowing phase exists for Model 1 with  $\theta_0 = -30^\circ$ , but the glide angle tends to an equilibrium value of about  $70^\circ$ . It can be also observed that the trajectory

of Model 1 with  $\theta_0 = 0^\circ$  reaches equilibrium in less than 1.5 s, while the experimental glide angle continues to decrease even after 2 s. On the other hand, the trajectories predicted by Model 2 change monotonically with  $\theta_0$ , and do not seem to reach equilibrium by the end of the simulation time; however, they underperform in horizontal distance traveled relative to both Model 1 and the experimental data.

The reason for the nonmonotonic behavior of Model 1 may be readily explained if we recall the following equation for the equilibrium glide angle:

$$\tan \gamma = \frac{C_d}{C_l} = f(\alpha) \tag{26}$$

where  $\alpha$  is the angle of attack, and  $f(\alpha)$  is a nonmonotonic function (see figure 1(F)).

The vertical and horizontal components of the velocity are also plotted in figures 4(C) and (D), respectively. As with the other performance metrics, it is clear that the simulated velocities do not closely match the experimental velocities. The velocities predicted by Model 2 have relatively similar trends to those of real snakes, for which the vertical velocity starts to increase in magnitude for roughly one second, after which sufficient airspeed is achieved and lift is generated to provide a positive vertical acceleration. Moreover, the horizontal velocity shows a positive acceleration during the whole time, although the acceleration starts to diminish after 1.5 s. However, the simulated velocities are considerably smaller in magnitude than the experimental data; whereas the largest vertical speed of snakes is  $\sim 6 \text{ m s}^{-1}$ , the simulated vertical speeds reach a maximum of  $\sim 4.5 \text{ m s}^{-1}$  (figure 4(C)). The velocity magnitude deficit is particularly obvious in the horizontal component of the velocities, which leads to the steep shallowing trajectories of Model 2 (figure 4(D)). The same discrepancies exist in the results of Model 1, in addition to the aberrant behavior of the vertical speed with  $\theta_0 = 0^\circ$ , where positive acceleration is never attained.

Figure 5 compares the recorded trajectory and pitch angle of a flying snake to the simulated ones obtained by integrating equations of motion of Model 2 from the same initial conditions. The experimental trajectory of the CoM, shown in figure 5(A), was calculated based on the 3D kinematic data of five landmarks on the snake body, recorded from the mid-to-end portion of the glide (Socha *et al* 2010). The experimental pitch angle, which was originally calculated using the same kinematic data, is repeated from figure 1(A). It can be seen that the simulated trajectory closely follows the recorded data; the maximum position difference between model and observed results was 13 cm over a total distance of more than 12 m traveled, resulting in a relative difference of 1.0%. On the other hand, the simulated pitch angle deviates largely from the recorded data. In particular, it seems that a phase shift exists between the two time series, although they exhibit the same dominant frequency, which is equal to the frequency of undulation. In addition, the amplitude of oscillations of the experimental pitch angle is roughly twice that of the simulated one.

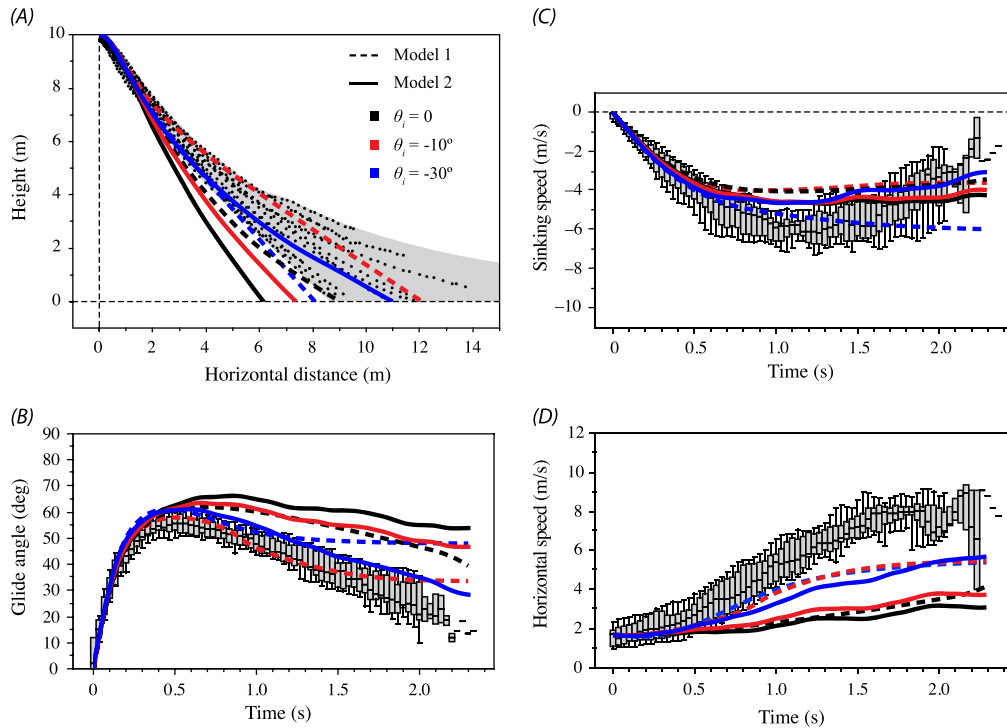


**Figure 4.** Comparison of the simulations with an assemblage of experimental data, from Socha *et al* (2005). (A) Trajectories and (B) associated glide angles produced by the theoretical models. The trajectories given by Model 1 (dashed lines) reach equilibrium earlier than real snakes, as can be seen in the glide angle data. In contrast, Model 2 (solid lines) produced trajectories that resemble experimental data, but underperform in terms of glide ratio. (C) and (D) show vertical and horizontal components of the velocity, respectively. Whereas both models are incapable of reaching velocities as high as seen in the snakes, Model 2 better predicts the trends in the velocities.

### 3.2. Stability analysis

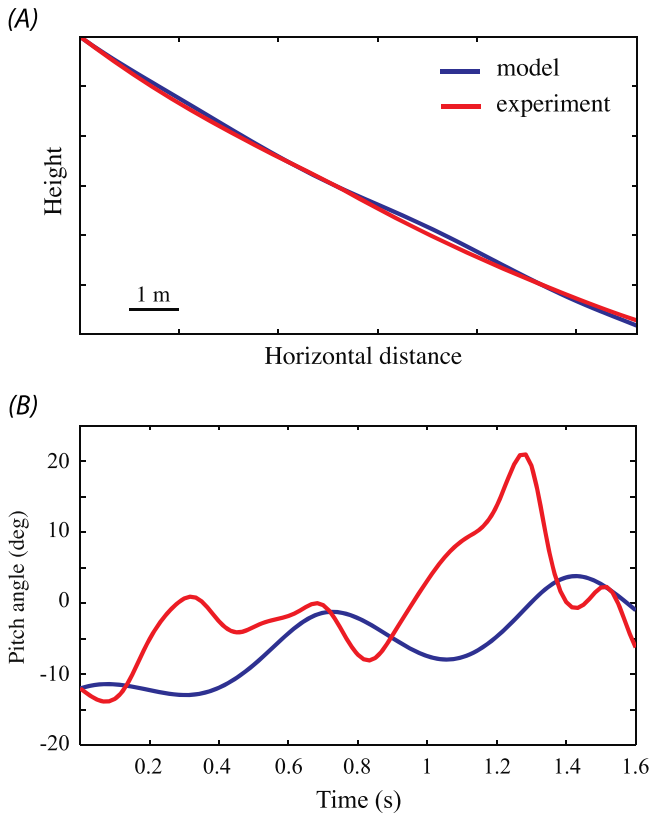
Model 1 was shown to have an equilibrium solution, although its equations of motion were nonautonomous. A trial-and-error investigation of the initial conditions revealed that the equilibrium of Model 1 is locally passively stable. The blue region in figure 6(A) shows the basin of stability of the equilibrium in the  $\theta_0 - \dot{\theta}_0$  plane, with the initial velocities set as the same as those of the experimental trajectories (see figure 4). It is clear that many of the snake-related initial conditions lie within the basin of stability of equilibrium. The trajectories that start from the initial conditions in blue go to the equilibrium state, whereas the initial conditions in red result in nongliding trajectories similar to those of a pure projectile (figure 6(B)).

To explore the stability properties of Model 2, the static stability criterion was first applied. As stated previously, this criterion provides a necessary condition only for stability of equilibrium solutions of a system. However, the steady-state response of Model 2 is periodic unless  $\Delta m$  is nullified; in other words, undulation effects had to be eliminated from the model for the stability criterion to be properly applied. Here, for the sake of comparison, we also examined the model with undulation by averaging its steady-state response over one period and applying the criterion to the averaged response. Finally, the effect of the controlling term  $K_u$  on stability of the model was examined by varying it from zero to its fitted value (table 2).

The results of the above analysis are given in figure 7(A). It is clear from the positive slope of the  $M_c - \alpha_b$  curves with

$K_u = 0$  that the model is unstable when no restoring moment acts on it. However, in all other cases, the slopes of the curves are negative, indicating that the restoring moment is capable of stabilizing the pitch dynamics, at least in the static sense. It is also important to note that undulation somewhat affects the  $M_c - \alpha_b$  curves; it slightly changes the slopes near the equilibrium point at  $\alpha_b \approx 26^\circ$ , and adds an unstable equilibrium point to the curve with  $K_u = 0.02$  Nm rad. However, it does not change the qualitative behavior of the curves near the stabilized equilibrium; therefore, the static stability analysis predicts that pitching stability cannot be achieved in Model 2 with  $K_u = 0$  just by switching undulation on or off.

The dynamic stability analysis of the periodic motions of Model 2 was also carried out using the Floquet theory. Figures 7(B)–(D) show all of the Floquet multipliers associated with six periodic solutions (each one resulting in eight Floquet multipliers) obtained by gradually changing a parameter of the model. The parameters of interest were the undulating amplitude index  $\zeta$  and the control indices  $K_u$  and  $B_u$ . We examined the effects of these parameters by varying them in the ranges  $0.1\zeta^{opt} < \zeta < \zeta^{opt}$ ,  $0.2K_u^{opt} < K_u < K_u^{opt}$ , and  $0.3B_u^{opt} < B_u < B_u^{opt}$ , one at a time. All other parameters of the model were kept fixed at their fitted values (table 2). When varying  $\zeta$ , we used  $K_u = 0.2K_u^{opt}$  instead of  $K_u = K_u^{opt}$ ; this choice was made to test if undulation could compensate when the control parameter was too small to provide stability on its own.



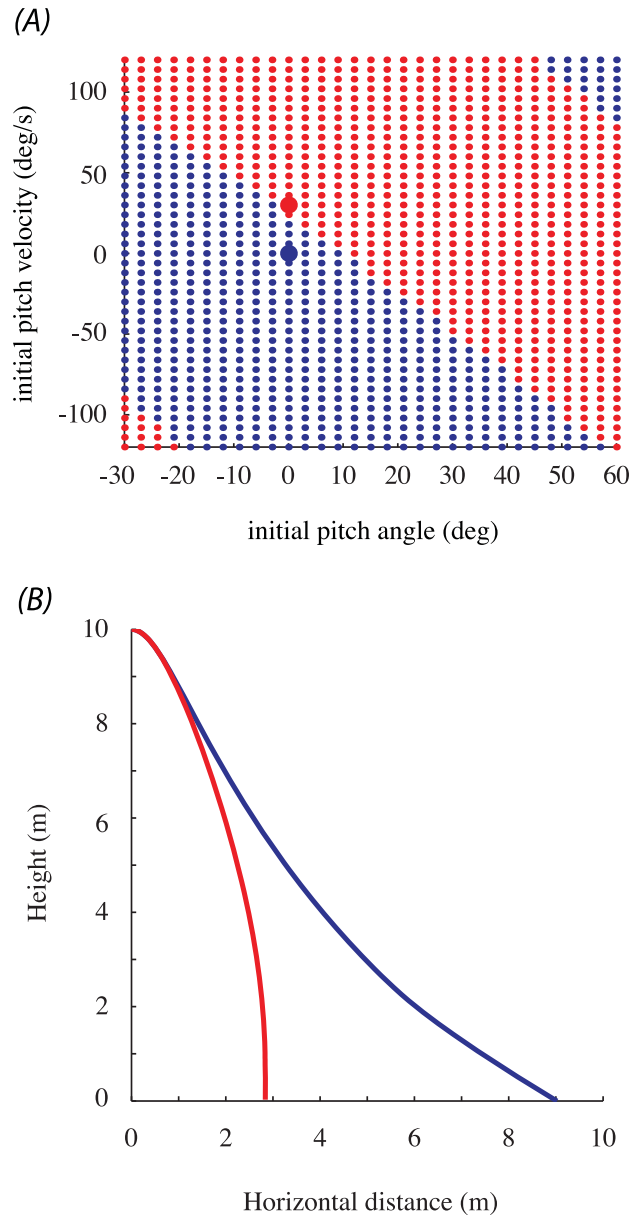
**Figure 5.** (A) Model 2 with the fitted parameters successfully reproduced the experimental average trajectory (Socha et al 2010). Because the data were from the late-phase gliding trajectory, no specific origin was selected for the plot, but only the displacements in the horizontal and vertical directions are shown. (B) The simulated pitch angle deviated from the experimental data. However, the two time series have the same dominant frequency, which is equal to the frequency of undulation.

Figure 7(B) shows that one of the Floquet multipliers enters the unit circle through +1 by increasing the undulation amplitude with  $\zeta > 0.1\zeta^{opt}$ , but the same multipliers later exits the unit circle through +1 when the undulation amplitude is further increased with  $\zeta > 0.9\zeta^{opt}$ . This means that undulation with amplitude bigger than a threshold could in fact compensate for the insufficient control parameter, but when the undulation amplitude increases beyond another threshold, it makes the model unstable again. Figures 7(C) and (D) show the effect of the control indices on the stability characteristics of the periodic motions. In figure 7(C), one of the Floquet multipliers enters the unit circle through +1 with  $K_u > 0.2K_u^{opt}$  and, in figure 7(D), one of the Floquet multipliers enters the unit circle through -1 with  $B_u > 0.3B_u^{opt}$ . This means that both control terms are required for a stable motion; also, there exist threshold values for these terms below which stability cannot be achieved.

#### 4. Discussion

##### 4.1. Stability analysis of the models

To investigate the theoretical stability characteristics of a flying snake during a glide trajectory, we developed two



**Figure 6.** The equilibrium solution of Model 1 is passively stable, with (A) basin of stability in the  $\theta_0 - \dot{\theta}_0$  plane, the initial velocity being  $(\dot{x}_0, \dot{z}_0) = (1.7, 0) \text{ m s}^{-1}$ . The trajectories starting from an initial condition within the blue region converge to equilibrium, whereas the initial conditions in red result in trajectories that do not shallow and are similar to those of projectiles. (B) Two representative trajectories starting from the initial conditions singularized in (A). See movies 1 and 2 for animations of the trajectories shown.

dynamical models. Model 1 was a simple representation of the staggered configuration of a gliding snake's body. Our analysis shows that the nonautonomous equations of motion of Model 1, indeed, had an equilibrium solution, which was locally passively stable. This counterintuitive result was an inherent feature of the model's structure, in which the uniform distribution of mass and pressure over the airfoils would cause the CoP and CoM to coincide and, therefore, the pitch equation to be identically satisfied. More interestingly, many

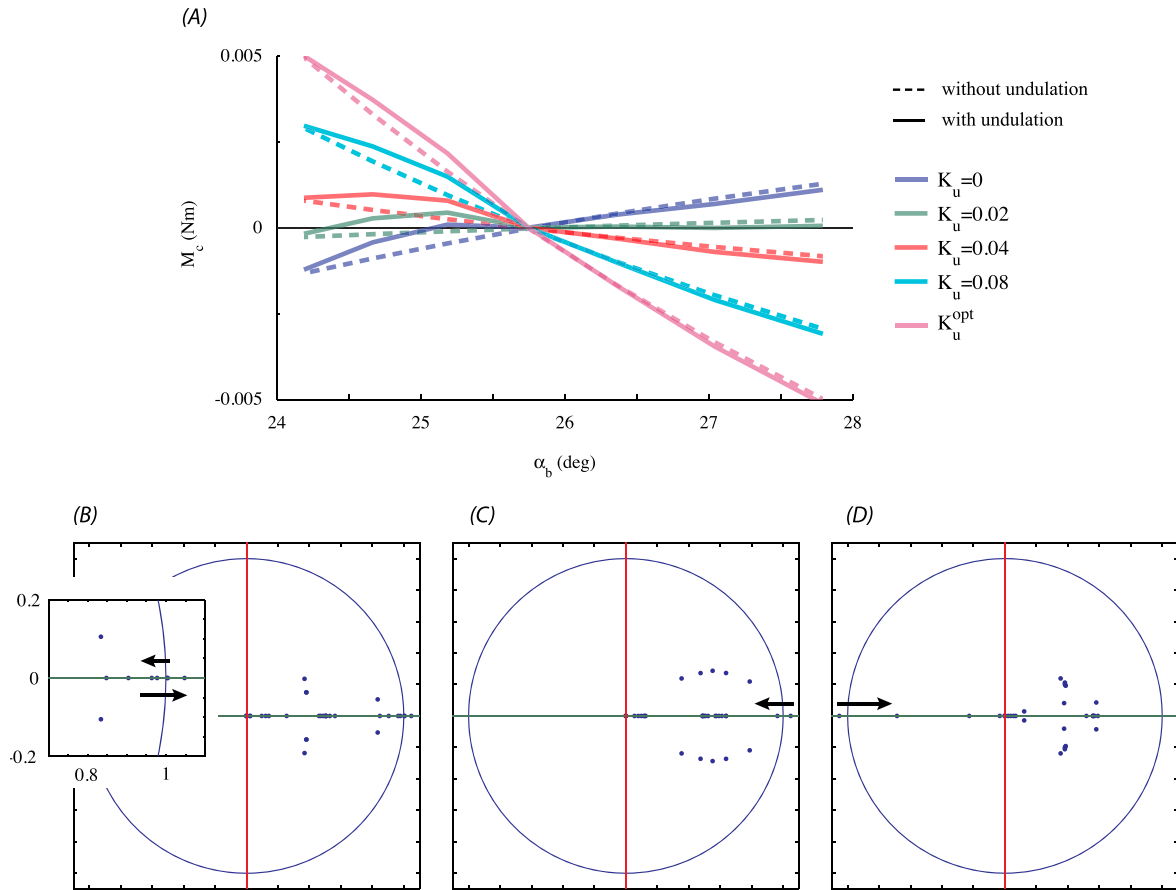


**Figure 7.** Results of the static (A) and dynamic (B-D) stability criteria applied to Model 2. (A) Plots of the pitching moment about the CoM,  $M_c$ , against the body angle of attack,  $\alpha_b$ , with different values of the control parameter  $K_u$ . The dashed lines and solid lines correspond to the model with no undulation ( $\zeta = 0$ ) and the model with undulation, respectively. These plots show that the model with  $K_u = 0$  is passively unstable, but becomes statically stable with a positive restoring moment. The Floquet multipliers (relative to the unit circle in the complex plane) associated with the periodic motions of Model 2 when (B)  $0.1\zeta^{opt} < \zeta < \zeta^{opt}$ , (C)  $0.2K_u^{opt} < K_u < K_u^{opt}$ , and (D)  $0.3B_u^{opt} < B_u < B_u^{opt}$ . The superscripts denote the fitted values of the parameters (table 2). The arrow in (B) shows that one of the Floquet multipliers enters the unit circle through +1 with  $\zeta > 0.1\zeta^{opt}$ , meaning that undulation compensates for a small control and stabilizes the motion (in this case, we set  $K_u = 0.2K_u^{opt}$ ). The arrows in (C) and (D) show that one of the Floquet multipliers enters the unit circle through +1 with  $K_u > 0.2K_u^{opt}$  and  $B_u > 0.3B_u^{opt}$ , respectively, meaning that an unstable motion could be stabilized using the restoring moment.

of the take-off conditions of flying snakes correspond to the initial conditions within the basin of stability of the equilibrium solution of Model 1. However, the structure of Model 1 requires that all parts of the virtual body contribute equally to producing aerodynamic forces, which is not possible in real gliding snakes due to variation of angle of attack and sweep angle along the body. Model 2 was developed to provide a more sophisticated representation of flying snake's behavior in mid-air. The airfoils were allowed to move with respect to each other; additionally, to account for potential control movements, a restoring moment was included to keep the pitch angle close to zero. This model was unstable in the pitch direction, but could be stabilized with the restoring moment.

An essential feature of snake gliding behavior that was incorporated into the models was undulation. *A priori*, undulation should affect the dynamics of flying snakes through at least three mechanisms: (i) continual changes in areas of the upstream and downstream airfoils, which in turn alters the aerodynamic forces; (ii) continual redistribution of

body mass, which changes the position of the CoM; (iii) inertial couplings between the translational and rotational motions (see equation (S21)). There are other possible effects of undulation; for instance, it may cause 3D unsteady aerodynamic interactions that are not observed in static measurements, and it has been postulated that it enables stability in the rolling direction (Socha and LaBarbera 2005), but this was not modeled here. These mechanisms motivated the hypothesis of this study that undulation contributes to stability in the pitch direction, which was tested by applying the Floquet theory to Model 2. As shown by figure 7(B), undulation with an amplitude properly adjusted between two limits can provide stability in the absence of sufficient control. However, the periodic solution was found to be unstable with  $K_u < 0.2K_u^{opt}$  or with  $B_u < 0.3B_u^{opt}$  regardless of the influences from undulation. This shows that undulation has a limited capability for providing stability.

The results of Model 2 suggest that flying snakes require active control to perform stable glides. Although the actual

control mechanisms that provide stability are not yet known, here we describe some possibilities. The asymmetric effect of pitch velocity on the airspeeds and angles of attack experienced by the upstream and downstream airfoils could be exploited to produce the restoring moment. This might be accomplished (see figure 3(A)) either by actively modifying  $r_1$  and  $r_2$ , or by actively oscillating the airfoils out of the model plane (i.e. the plane defined by the line connecting the airfoils). Both of these mechanisms would change the magnitude and direction of the airfoils' velocities and could be used as means of control. Another potential mechanism could take advantage of the dynamic changes of the aerodynamic load distribution along the snake body. This is in part supported by the results of preliminary tandem model manipulations, which suggest that changing the horizontal gap and vertical stagger affects the lift and drag forces on both airfoils (Miklasz *et al* 2010). In some configurations of the tandem models, the lift and drag coefficients of the downstream airfoil are about half of those of the upstream airfoil, but the force coefficients approached those of a solitary airfoil when moved apart by multiple chord lengths. Thus, a 'nose-down' pitching moment could be produced in Model 2 by moving the downstream airfoil farther downstream (increasing  $r_2$ ), while a 'nose-up' pitching moment requires the opposite movement. Although damping could also be obtained with a similar strategy, it should be recognized that some amount of damping is inherent in the dynamics of Model 2, which originates from the asymmetric effect of pitching velocity on the velocities of the upstream and downstream airfoils. This gives rise to a force asymmetry and a counteracting moment is thereby produced.

Recalling that the flying snakes produce lift using their entire body as a morphing wing, it becomes clear that one functional consequence of the S-shape is that it creates 'upstream' and 'downstream' airfoils. In fact, Miklasz *et al* (2010) found that an enhancement in overall lift-to-drag ratio might be achieved with certain configurations. Thus, forming the staggered S-shape may enable such aerodynamic interactions. Moreover, it is well known that no aircraft could be made with a single positively cambered wing, because it would be unstable in the pitching direction (Etkin 1972). In practice, such wings may be used only in conjunction with an auxiliary surface that provides a nose-up moment when the wing is at zero lift. This may explain another possible function of the aerial snake's S-shape.

#### 4.2. Implications about gliding snakes

The seemingly contradictory results of our two models, when viewed together, render a deeper insight of how the control system of flying snakes works. Model 1 indicates that there exists a passively stable equilibrium state to which the trajectories converge, provided that they start from proper initial conditions within the basin of stability. Therefore, flying snakes would be able to glide without need for closed-loop feedback control if they could reconfigure their body according to the kinematics of Model 1. However, closed-loop feedback control is likely necessary, resulting from

several idealizations in Model 1: (i) the couplings between the longitudinal and lateral motions have been neglected, (ii) mass and aerodynamic forces were distributed uniformly over the body area and, (iii) segments of the body are rigidly coherent. These criteria can never be met by an animal glider. Nonetheless, the ideally passively stable trajectory predicted by Model 1 provides an underlying 'dynamical skeleton' for closed-loop control to work with. A similar framework has been developed for walking in bipeds, which was believed to require active control. However, passively stable gaits have been found in theory, and these have been used to develop passive biped walkers (e.g. Garcia *et al* 1998, Collins *et al* 2005).

The results of Model 2 provide the basis for predictions of how a snake's sensory system should provide feedback on body position and orientation while airborne. The success of Model 2 in predicting stable glide trajectories with a restoring moment proportional to the pitch angle, along with the observation that flying snakes tend to remain level with the ground during gliding, supports the idea that the snakes use pitch angle as a feedback variable in a closed-loop control system. Indeed, both the vestibular and/or visual systems are viable candidates for providing the primary sensory information needed for such control. Boistel *et al* (2011) observed that dimensions of the vestibular system in species of squamates capable of descent in the air were different from those in species with only a climbing or terrestrial lifestyle, and suggested that these modifications might be related to the maintenance of stability. Interestingly, the vision of flying snakes has been implicated as being particularly acute compared to that of other snake species (Socha and Sidor 2005), which may suggest a role in providing visual input to the animal's control system.

This does not exclude the possibility of other measures of position and orientation being utilized as feedback signals; for example, proprioception and pressure distribution information from the skin could provide sensory information. Nonflying snakes are known to possess mechanoreceptors that include rapidly adapting receptors and slowly adapting receptors (Proske 1969). However, rapidly adaptive receptors have high mechanical thresholds and restricted receptive fields. If flying snakes use skin pressure for feedback, they would require fast responses to small changes in air pressure. Assuming an ability to sense differences in flow speed on the  $\text{dm s}^{-1}$  scale, this would require mechanoreceptors with a sensitivity on the order of  $10^{-2}$  Pa.

#### 4.3. Gliding trajectories

The theoretical models of this study were based on experimental data from the developed stage of the glide. Our simulations of gliding trajectories (figure 4) were conducted with the assumption that the models represented the behavior of flying snakes both in the ballistic dive and shallowing phases. However, the initial ballistic dive involves postural configurations whose effects have not been quantitatively studied. Starting with a straight body, during this phase the snake forms the S-shape and pitches downward (Socha 2002),

bringing itself to the staggered configuration shown in figure 1(C). Therefore, it is likely that the aerodynamic forces acting on the snake are different in the ballistic dive phase. This might explain why both models predicted trajectories with speeds whose magnitudes are much less than those achieved by gliding snakes (figures 4(C) and (D)). Furthermore, Model 2 predicted trajectories that became closer to the measured data when the initial pitch angle was changed from 0° to -30° (figures 4(A) and (B)). By decreasing the initial pitch angle, the model would benefit from smaller angles of attack in the ballistic phase to decrease drag and to obtain greater glide speed by the beginning of the shallowing phase; greater speed would result in greater lift production. Because the restoring moment would increase the angle of attack by making the pitch angle tend to zero, smaller initial pitch angles should produce trajectories that are more realistic.

#### 4.4. Conclusions

This study presents two new first-order dynamical models developed to understand the gliding performance of flying snakes, in particular, the stability of the snake about the pitch axis. Model 1, which was a simple two-dimensional representation of the airborne snake as three rigidly attached airfoils, resulted in equilibrium glide trajectories that were locally passively stable. However, with relaxation of the rigidity assumption and other essential features of the gliding snake incorporated into Model 2, the passive stability was lost. It was then shown that the trajectories of Model 2 could be stabilized with a simple control mechanism using the pitch angle and pitch velocity as feedback. Although the modeling in this study was motivated as an attempt to understand how flying snakes glide, these results may be broadly applicable to a wide array of staggered, multi-winged flyers, at least within the low Reynolds number regime used by the snakes. Our initial first-order modeling also suggests that flying snakes require active control for stable gliding, but caution is warranted in over-extending these results to real gliding flight. Verification of the theoretical models using physical experiments is needed, and a full exploration of the parameter space should be conducted to probe the limits of the system. Furthermore, the biomechanical properties of the snake's body, as well as body orientation angles and muscle activity during gliding, must be measured to understand its control parameters. If experimentally justified, Model 2 would become a powerful tool to study the dynamics of flying snakes, and can be used to examine those aspects of gliding that are difficult, if not impossible, to study experimentally.

#### Acknowledgements

This research was partially supported by DARPA grant W911NF1010040 to JJS and PPV. SDR gratefully acknowledges partial support by the National Science Foundation under Grant No. CMMI-1150456.

#### References

- Alexander R M 2003 *Principles of Animal Locomotion* (Princeton, NJ: Princeton University Press)
- Biewener A A 2003 *Animal Locomotion* (New York: Oxford University Press)
- Bishop K L 2006 The relationship between 3D kinematics and gliding performance in the southern flying squirrel, *Glaucomys volans* *J. Exp. Biol.* **209** 689–701
- Boistel R, Herrel A, Lebrun R, Daghfous G, Tafforeau P, Losos J B and Vanhooydonck B 2011 Shake rattle and roll: the bony labyrinth and aerial descent in squamates *Int. Comp. Biol.* **51** 957–68
- Cheng B, Deng X and Hedrick T L 2011 The mechanics and control of pitching manoeuvres in a freely flying hawkmoth (*Manduca sexta*) *J. Exp. Biol.* **214** 4092–106
- Collins S, Ruina A, Tedrake R and Wisse M 2005 Efficient bipedal robots based on passive-dynamic walkers *Science* **307** 1082–5
- Dudley R 2002 Mechanisms and implications of animal flight maneuverability *Int. Comp. Biol.* **42** 135–40
- Etkin B 1972 *Dynamics of Atmospheric Flight* (New York: Wiley)
- Gao N, Aono H and Liu H 2011 Perturbation analysis of 6 DoF flight dynamics and passive dynamic stability of hovering fruit fly *Drosophila melanogaster* *J. Theor. Biol.* **270** 98–111
- Garcia M, Chatterjee A, Ruina A and Coleman M 1998 The simplest walking model: stability, complexity, and scaling *ASME J. Biomech. Eng.* **120** 281–8
- Heyer W R and Pongsapipatana S 1970 Gliding speeds of *Ptychozoon lionatum* (Reptilia: Gekkonidae) and *Chrysopelea ornata* (Reptilia: Colubridae) *Herpetologica* **26** 317–9
- Holden D, Socha J J, Cardwell N and Vlachos P P 2014 Aerodynamics of the flying snake, *Chrysopelea paradisi*: how a bluff-body cross-sectional shape contributes to gliding performance *J. Exp. Biol.* **217** 382–94
- Krishnan A, Socha J J, Vlachos P P and Barba L A 2014 Lift and wake of flying snakes *Phys. Fluids* **26** 031901
- McCay M G 2001 Aerodynamic stability and maneuverability of the gliding frog *Polypedates dennysi* *J. Exp. Biol.* **204** 2817–26
- McCormick B W 1976 *Aerodynamics, Aeronautics and Flight Mechanics* (New York: Wiley)
- McGuire J 1998 Phylogenetic systematics, scaling relationships and the evolution of gliding performance in flying lizards (Genus *Draco*) *PhD Thesis* University of Texas
- Miklasz K, LaBarbera M, Chen X and Socha J J 2010 Effects of body cross-sectional shape on flying snake aerodynamics *Exp. Mech.* **50** 1335–48
- Nayfeh A H and Balachandran B 2004 *Applied Nonlinear Dynamics* (Weinheim: Wiley)
- Proske U 1969 An electrophysiological analysis of cutaneous mechanoreceptors in a snake *Comp. Biochem. Physiol.* **29** 1039–46
- Scholey K 1986 The climbing and gliding locomotion of the giant red flying squirrel *Petaurista petaurista* (Sciuridae) *Bat Flight: Fledermausflug* ed W Nachtigall (Stuttgart: Gustav-Fischer) pp 187–204
- Socha J J 2011 Gliding flight in *Chrysopelea*: turning a snake into a wing *Int. Comp. Biol.* **51** 969–82
- Socha J J 2002 Gliding flight in the paradise tree snake *Nature* **418** 603–4
- Socha J J and LaBarbera M 2005 Effects of size and behavior on the aerial performance of two species of flying snake (*Chrysopelea*) *J. Exp. Biol.* **208** 1835–47
- Socha J J, Miklasz K, Jafari F and Vlachos P P 2010 Non-equilibrium trajectory dynamics and the kinematics of gliding in a flying snake *Bioinspir. Biomim.* **5** 045002
- Socha J J, O'Dempsey T O and LaBarbera M 2005 A 3D Kinematic analysis of gliding in a flying snake, *Chrysopelea paradisi* *J. Exp. Biol.* **208** 1817–33



- Socha J J and Sidor C A 2005 *Chrysopelea ornata*, *C. paradisi* (flying snakes): behavior *Herp. Rev.* **36** 190–1
- Taylor G K and Thomas A L R 2002 Animal flight dynamics: II. Longitudinal stability in flapping flight *J. Theor. Biol.* **214** 351–70
- Taylor G K and Thomas A L R 2003 Dynamic flight stability in the desert locust *Schistocerca gregaria* *J. Exp. Biol.* **206** 2803–29
- Thomas A L R and Taylor G K 2001 Animal flight dynamics: I. Stability in gliding flight *J. Theor. Biol.* **212** 399–424